nature energy

Article

https://doi.org/10.1038/s41560-026-02015-8

Amorphous self-assembled multilayers for perovskite solar cells with improved reverse bias stability

Received: 19 August 2025

Accepted: 24 February 2026

Published online: 20 March 2026

Check for updates

Qifan Feng[1,9], Kai-Kai Liu[2,3,9], Deng Wang[2,3,9], Songyang Yuan[2], Zhenhuang Su[4], Zhaoyu Lou[1], Ziwei Liu[1], Nikhil Kalasariya[1], Wenlin Jiang[2,3], Xin Wu[5], Shuo Zhang[6], Binghui Wu[7], Zonglong Zhu[5], Xiaofeng Huang[2,3] ✉, Alex K.-Y. Jen[2,3,5,8] ✉ & Martin Stolterfoht[1] ✉

Robust hole-selective interfaces are critical for the stability of perovskite solar cells, yet this requirement is inadequately addressed by self-assembled monolayers (SAMs). Here we combine (4-(7*H*-dibenzo[*c*,*g*]carbazol-7-yl)butyl)phosphonic acid (CbzNaph) and its hydroxyl functionalized analogue (CbzNaphOH), which features intramolecular hydrogen-bonding interactions between the spacer and anchoring groups, to modulate SAM molecular packing. Increased steric hindrance promotes the formation of an amorphous self-assembled multilayer (a-SAMUL) with homogeneous packing. This amorphous layer acts simultaneously as a uniform, strongly adhesive binding medium that tightly couples the perovskite and substrate—thereby suppressing the formation of mobile ions—and as an efficient hole-selective contact with favourable energy-level alignment. Devices incorporating a-SAMULs achieve a certified efficiency exceeding 26% and reduced ion-migration-driven degradation. The devices exhibit reverse breakdown voltages exceeding −17 V and maintain operational stability for over 3,000 h with negligible degradation. These findings underscore the effectiveness of a-SAMULs in enhancing the long-term reliability of perovskite photovoltaics.

Metal halide perovskite solar cells (PSCs) have achieved certified power conversion efficiencies (PCEs) approaching 27% (refs. 1–3), representing an important milestone in photovoltaic research. However, long-term stability remains a critical challenge impeding commercial deployment, primarily due to the intrinsic ionic instability of perovskites under external stimuli[4,5]. In particular, while degradation caused by oxygen and moisture can be largely mitigated by physical encapsulation[6], ion-migration-induced degradation persists under illumination[7], heating[8] and electrical bias[9]. This phenomenon compromises device stability across multiple dimensions: first, by increasing defect density within the perovskite lattice; second, by altering film morphology; third, by inducing interfacial field screening; fourth, by degrading charge-transporting layers (CTLs); and finally, in severe cases, by causing material decomposition and corroding the electrode materials[10–14]. These effects collectively highlight a strong correlation between PCE losses and the presence and mobility of ionic species within the perovskite layer[15].

This issue is particularly crucial under reverse bias conditions, which commonly occur in series-connected modules when individual subcells experience elevated reverse voltages—often due to partial shading or localized short circuits—leading to the sequential breakdown of adjacent subcells[16]. Once the reverse voltage exceeds a certain threshold, the current increases sharply. This abrupt increase defines the reverse breakdown voltage (V_{rb}) (Methods). Before V_{rb}, the applied

A full list of affiliations appears at the end of the paper. ✉e-mail: xhuan7@cityu.edu.hk; alexjen@cityu.edu.hk; mstolterfoht@ee.cuhk.edu.hk

reverse bias can drive halide ions to accumulate at the perovskite–CTL interface, inducing substantial band bending that facilitates tunnelling of minority carriers from the CTL into the perovskite layer[17]. This tunnelling process not only oxidizes halide ions but also increases the risk of external ions (for example, oxidized cathode) diffusing into the perovskite layer[18]. Once metal ions migrate across the device to the anode, rapid degradation and eventual short-circuiting may occur. To mitigate these effects, various metal oxides have been incorporated as buffer layers[19,20], in either direct or indirect contact with the perovskite top surface[21], to suppress ion migration and improve reverse bias stability[22]. However, limited attention has been given to the role of the hole-selective interface in ion-migration-related perovskite degradation and device stability[9]. Beyond serving as efficient hole-transporting materials (HTMs), these interlayers must also function as effective ion migration barriers to prevent direct contact between the perovskite and the anode substrate. Such contact can create severe leakage pathways, facilitate non-radiative recombination and trigger interfacial chemical reactions that compromise the structural integrity of the perovskite layer.

Nonetheless, both commonly used HTMs and emerging carbazole-based hole-selective layers (HSLs) face persistent challenges in achieving favourable bidirectional molecular contact with both the perovskite and the anode interface. Conventional HTMs often suffer from poor interfacial contact and chemical incompatibility; for instance, the hydrophobic surface of poly[bis(4-phenyl)(2,4,6-trimethylphenyl)amine] (PTAA) usually introduces buried pinholes, whereas redox-active Ni^{2+}/Ni^{3+} species in NiO_x can accelerate perovskite degradation. Although ultrathin HSLs based on π-conjugated SAMs enable efficient charge transport via tunnelling, they often fail to form uniform and stable anchoring on the anode substrate[23]. In addition, their strong aggregation tendency and weak interfacial interactions exacerbate interfacial heterogeneity[24], leading to potential shunting pathways that promote ion migration. As a result, state-of-the-art devices using SAM-based HSLs typically exhibit relatively low V_{rb} values of only −1 to −2 V (Supplementary Fig. 1). However, devices incorporating thicker polymeric HTMs (for example, PTAA) with effective leakage current suppression achieve higher V_{rb} values (that is, more negative than −10 V) but at the expense of reduced PCE, reflecting a trade-off between efficiency and stability[9]. Currently, this level of reverse bias tolerance remains insufficient to allow the usage of established, cost-effective silicon-based bypass diode strategies (for example, 24 cells per diode), which typically activate at reverse biases across a shadowed subcell of −15 to −20 V (refs. 25,26). To ensure the protection of a perovskite solar module, the target breakdown voltage must be slightly more negative than this threshold voltage; otherwise, irreversible device failure occurs before diode engagement. Therefore, a thorough understanding of the structure-property relationship of hole-contact interlayers—particularly their influence on ion-induced efficiency loss and reverse bias stability—is essential for clarifying the degradation mechanisms in PSCs[27].

In this work, we identify molecular contact at the hole-selective interlayer as a critical factor governing the limited reverse bias stability and mobile ion-induced degradation losses in PSCs. To address this, we develop an amorphous self-assembled multilayer (SAMUL) strategy to effectively tailor bidirectional molecular contact between the perovskite and the anode substrate. The resulting amorphous SAMUL forms a robust anode-binding monolayer and a homogeneously dispersed overlayer, serving as an efficient hole-selective interlayer, but also a reliable barrier against leakage, a strong interfacial binder to the perovskite and a platform for uniform perovskite growth. This approach yields devices with a certified PCE of 26.3%, substantially reduced ion-migration-induced losses, and reverse bias breakdown voltages exceeding −17 V. Notably, devices incorporating this optimized amorphous SAMUL architecture retained nearly 100% of their initial PCE after 3,000 h of continuous operation, demonstrating exceptional long-term stability.

Results and discussion

Optimization of hole-contact interlayers

To assess the impact of ion migration on the hole-transporting side of PSCs, devices with the architecture ITO/HTM or HSL/perovskite/C_{60}/BCP/Ag (where BCP is bathocuproine) were fabricated. A pure-iodide perovskite composition ($FA_{0.85}MA_{0.1}Cs_{0.05}PbI_3$) was used as the light-absorbing layer, while C_{60} and BCP functioned as the electron-transporting layers. Previously developed fast-hysteresis (FH) current density–voltage (*J*–*V*) measurements were utilized to quantify the effect of mobile ions on device performance[28]. Details of the method are provided in the Methods. In brief, FH measurements can evaluate both steady-state and ion freeze-state efficiencies by comparing device performance under slow and rapid scan rates. When the fast scan rate greatly exceeds the ion diffusion rate, ionic motion is effectively frozen (Fig. 1a), allowing the estimation of ionic losses due to electric-field screening effects[12,29]. Ionic loss is defined as $L_{ion} = n_{ion\text{-}freeze} - n_{steady\text{-}state}$.

The hole-contact interfaces of commonly used HTMs, including organic PTAA polymers and inorganic NiO_x, as well as carbazole-based SAMs, including 2PACz, 4PACz, Me-4PACz and CbzNaph, were systematically compared[24,30–35] (Fig. 1b). Conventional HTMs with favourable electrical properties enable the use of relatively thick films to achieve full substrate coverage without compromising hole transport. Consequently, devices using optimized HTM concentrations show reduced ion-induced losses (L_{ion}: 6.6% for PTAA and 8.3% for NiO_x; Supplementary Figs. 2 and 3), albeit with relatively low PCEs of 21.2% and 20.1%, respectively. Nevertheless, carbazole-based devices generally show poorer suppression of ionic losses than PTAA-based devices, with ionic losses of 15.6%, 23.3% and 14.7% for 2PACz, 4PACz and Me-4PACz, respectively (Supplementary Figs. 4–6). The increased ionic losses may result from the antiparallel molecular packing of these SAMs, which limits π–π stacking between adjacent carbazole units[32] (Fig. 1c). Moreover, loose molecular packing and insufficient contact with the substrate during film formation can lead to incomplete interfacial coverage, thereby increasing the risk of direct perovskite–anode contact (Fig. 1d, schematic diagram).

In comparison, the helical π-expansion SAM, CbzNaph, featuring a 7*H*-dibenzo[c,g]carbazole unit, exhibits a lower ionic loss of 10.3%—comparable to that of conventional HTMs—while achieving a higher PCE of 22.7% (Supplementary Fig. 7). This enhanced performance arises from its enhanced π-stacked packing motif (Fig. 1c, schematic diagram), where strong π–π overlap promotes the formation of a highly ordered one-dimensional assembly along the *c*-axis. As discussed below, this structure enables the formation of a SAMUL at higher concentrations, consisting of a substrate-contacting monolayer and a buried perovskite-contacting overlayer. This architecture supports efficient charge transport while preventing direct perovskite–anode contact. However, the moderate concentration-dependent performance of CbzNaph-based devices (Fig. 1g and Supplementary Table 1) suggests suboptimal molecular assembly and inhomogeneous aggregate dispersion within the overlayer, which can impair hole-selective performance (Fig. 1e). To address this limitation, a CbzNaph derivative (CbzNaphOH) was designed by introducing a hydroxyl group onto the spacer linker of CbzNaph (synthetic details and characterizations are provided in the Methods, Supplementary Scheme 1 and Supplementary Figs. 8–15). CbzNaphOH was subsequently combined with CbzNaph to modulate molecular aggregation and promote the formation of a co-SAMUL interlayer. The resulting co-SAMUL exhibits improved concentration tolerance when used as the HSL compared with CbzNaph alone (Fig. 1h). These results imply the improved assembly in both the monolayer and overlayer, thereby enhancing interfacial hole selectivity (Fig. 1f, schematic diagram). The underlying mechanism is discussed in the following sections.

Given that the hydroxyl-rich surface of NiO_x facilitates SAM anchoring[34], and that SAM treatment can simultaneously prevent direct interaction between the reactive NiO_x surface and the perovskite[36,37]

https://doi.org/10.1038/s41560-026-02015-8

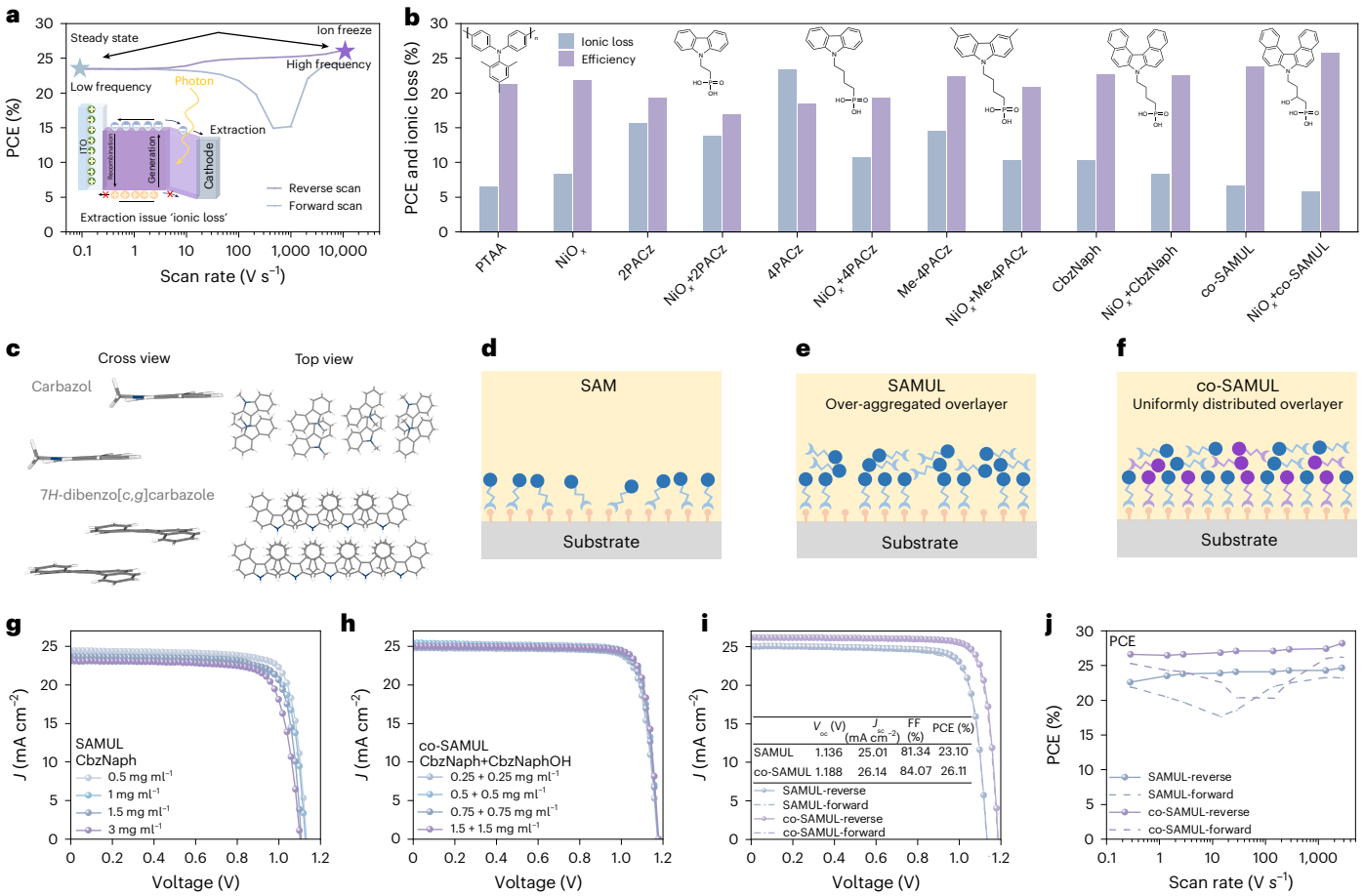

Fig. 1 | Optimization of hole-selective contacts for high-performance PSCs. **a**, Schematic illustration of the FH measurement and the associated field-screening effect. The blue star denotes device performance measured at low scan frequency, where the slow scan rate allows mobile ions to migrate and accumulate at the interfaces, resulting in ionic losses. The purple star represents the performance at high scan speeds, where the rapid voltage sweep effectively freezes ionic motion. The inset shows a schematic band diagram of the device. The purple region represents the perovskite layer, the light-blue area on the left corresponds to the anode, and the grey area on the right denotes the cathode. Incident photons generate electron–hole pairs within the perovskite; electrons (blue '−' circles) are extracted towards the metallic cathode, and holes (orange '+' circles) are extracted towards the ITO anode, while green spheres ('+' circles) indicate mobile ions contributing to ionic loss. **b**, Device performance as a function of the hole-selective interface, showing the relative ionic loss and the corresponding PCE. From left to right, the hole-selective materials are PTAA, (2-(9*H*-carbazol-9-yl)ethyl)phosphonic acid (2PACz), 4-(9*H*-carbazol-9-yl) phenylphosphonic acid (4PACz), [4-(3,6-dimethyl-9*H*-carbazol-9-yl)butyl] phosphonic acid (Me-4PACz), CbzNaph, and CbzNaphOH. **c**, Molecular packing motifs of the representative carbazole and 7*H*-dibenzo[c,g]carbazole units in the SAM and SAMUL structures, respectively. **d**–**f**, Schematic illustration of SAM (**d**), SAMUL (**e**) and co-SAMUL (**f**) aggregation modes on the substrate. The grey bar represents substrate, with yellow round-headed rods symbolizing surface hydroxyl groups. The blue and purple molecular structures correspond to CbzNaph and CbzNaphOH molecules, respectively. **g**,**h**, Concentration-dependent device performance using CbzNaph (**g**) and CbzNaph/CbzNaphOH (**h**) composites as HSLs. **i**, Champion performance of the devices incorporating NiO_x combined with CbzNaph or co-SAMUL as HTLs. J_{sc} denotes the current density; V_{oc} denotes the voltage; and FF denotes the fill factor. **j**, Evolution of ionic losses in the optimized device, extracted from *J*–*V* measurements conducted at varying scan speeds.

(Supplementary Fig. 16), we further investigated a composite structure combining NiO_x with SAM or SAMUL as a representative hole-contact interlayer for performance optimization. As expected, this NiO_x/co-SAMUL configuration enhances the device efficiency, yielding a champion PCE of 26.1% and a certified PCE of 26.3% from an independent certification institution (Fig. 1i and Supplementary Fig. 17), while reducing L_{ion} to 5.7% (Fig. 1j and Supplementary Fig. 18). In addition, co-SAMUL-based devices notably outperform their SAM and SAMUL counterparts on NiO_x in suppressing ionic losses (L_{ion}: 13.7%, 10.7%, 10.3% and 8.3% for 2PACz, 4PACz, Me-4PACz and CbzNaph, respectively; Supplementary Figs. 19–22). Further analysis reveals a solid correlation between ionic loss and device efficiency (Supplementary Fig. 23 and Supplementary Table 2). Moreover, this approach demonstrates broad applicability across devices incorporating composition- and bandgap-tailored perovskites (Supplementary Figs. 24–28). These findings highlight the critical role of interfacial contact optimization and molecular packing control in SAMUL design to improve device performance and suppress ion-migration-induced losses.

Molecular stacking of SAMULs

To elucidate the performance differences among SAMUL-based devices, we conducted a comparative analysis of molecular structures, self-assembled aggregates, and the corresponding electro-optical film properties. X-ray diffraction (XRD) measurements reveal that both CbzNaph and CbzNaphOH powders exhibit good crystallinity in the solid state (Supplementary Fig. 29). However, spin-coated HSL films derived from these materials display no distinct crystalline features, probably due to weak diffraction signals from self-assembled films, as confirmed by both XRD (Supplementary Fig. 30) and grazing-incidence wide-angle X-ray scattering (GIWAXS; Supplementary Fig. 31). To further probe their assembly behaviour, films were prepared by drop-casting under slow solvent evaporation conditions. CbzNaph

forms inhomogeneous, highly crystalline aggregates, whereas CbzNaphOH and the co-SAMUL yield uniform, predominantly amorphous aggregates (Supplementary Fig. 32). Diffraction analyses further validated these phase characteristics. CbzNaph exhibits sharp diffraction spots (Fig. 2a,b) with two sets of peaks, corresponding to two distinct packing motifs between adjacent π-expanded carbazole units. By contrast, CbzNaphOH and co-SAMUL show markedly reduced crystallinity, consistent with amorphous aggregation, as further supported by XRD analysis (Supplementary Fig. 33).

A series of molecular characterizations was performed to investigate how hydroxyl functionalization of the CbzNaph linker modulates molecular aggregation, despite the intrinsically strong π–π interactions of the 7*H*-dibenzo[c,g]carbazole unit. Density functional theory (DFT) calculations (Supplementary Fig. 34) reveal similar dihedral angles in the π-expanded carbazole cores of CbzNaph and CbzNaphOH, but notable geometric differences in their linker regions. In particular, CbzNaphOH adopts a torsional conformation between the linker and the phosphonic acid anchor, enabling the formation of a strong intramolecular hydrogen bond between the hydroxyl group and the phosphoric acid moiety. This interaction is expected to generate a six-membered ring conformation lock, an interpretation supported by the observed shift in the P=O stretching vibration upon hydroxyl incorporation (Supplementary Fig. 35).

The presence of a stable intramolecular hydrogen-bonded conformation in CbzNaphOH is supported by comprehensive nuclear magnetic resonance (NMR) analyses. Comparative ^{1}H NMR spectra acquired in dimethyl sulfoxide (DMSO)-d_6 reveal that hydroxyl substitution at the C3 position induces a pronounced chemical shift difference ($\Delta\delta$) between the diastereotopic methylene protons H_b and $H_{b'}$ (Fig. 2c, enlarged view). This splitting indicates restricted rotation about the C2–C3 bond, placing H_b and $H_{b'}$ in distinct magnetic shielding environments[38]. In conjunction with infrared spectroscopic evidence, these observations are consistent with the formation of a six-membered intramolecular hydrogen-bonded conformation involving the C3 hydroxyl group and the phosphoryl moiety, which stabilizes a well-defined molecular geometry. Further insight is provided by variable-temperature ^{1}H NMR studies[39,40], where the chemical shift differences of both the $H_b/H_{b'}$ and $H_d/H_{d'}$ proton pairs progressively decrease with increasing temperature (Fig. 2d, enlarged view). This temperature-dependent signal convergence reflects thermally activated conformational averaging, indicative of a gradual weakening of the intramolecular hydrogen-bonding interaction and relaxation of the associated conformational constraints. Importantly, ^{1}H NMR spectra recorded over a 20-fold concentration range exhibit negligible spectral changes (Supplementary Fig. 36), confirming the intramolecular origin of this interaction and excluding contributions from intermolecular hydrogen bonding. Complementary investigations using diethyl (4-(7*H*-dibenzo[c,g]carbazol-7-yl)-3-hydroxybutyl)phosphonate in low-polarity $C_2Cl_4D_2$ further corroborate this interpretation (Supplementary Fig. 37). Similar temperature-dependent spectral evolution, characterized by progressive signal averaging and complete thermal reversibility, is observed, indicating that the intramolecular hydrogen-bonded conformation is preserved across different solvent environments and chemical substitutions. Collectively, these results consistently verify the presence of a persistent yet thermally reversible intramolecular hydrogen-bonded structure in CbzNaphOH.

Subsequently, the effect of linker design on molecular packing was investigated through molecular simulations. Both CbzNaph and CbzNaphOH adopt two distinct packing orientations; however, they exhibit markedly different conformational characteristics (Fig. 2e and Supplementary Fig. 38). In CbzNaph, molecular packing is dominated by synergistic π–π interactions between the aromatic headgroups. The flexible butyl linker accommodates multiple conformations, enabling efficient π–π overlap and a close stacking distance between adjacent aromatic units. By contrast, hydroxyl functionalization in CbzNaphOH provides an additional hydrogen-bonding site that enforces conformational locking of the alkyl spacer. This hydrogen-bond-induced rigidity restricts spacer flexibility and constrains the relative orientation of the aromatic headgroups, limiting the optimization of π–π stacking. Consequently, the rigidified spacer increases the π–π separation between neighbouring aromatic units and disrupts the original packing motif, leading to reduced structural order and diminished crystallinity. In the CbzNaph/CbzNaphOH mixture, the competition between π–π-driven aggregation and hydrogen-bond-induced conformational locking suppresses long-range molecular order, yielding a co-SAMUL aggregate that approaches an amorphous packing state. A similar aggregation transition is observed for the Me-4PACz/CbzNaphOH blend compared with crystalline Me-4PACz[11,36] (Supplementary Fig. 39). These findings highlight the critical role of non-covalent-interaction-induced conformational locking in modulating molecular packing and preventing excessive crystallization.

Building on the understanding of molecular packing in SAMULs, we further examined their interfacial heterogeneity, which governs molecular contact between the anode substrate and the buried perovskite layer. In this discussion, we focus on crystalline CbzNaph (c-SAMUL) and the amorphous CbzNaph/CbzNaphOH composite (a-SAMUL). Mechanical adhesion tests at both the SAMUL/anode substrate and SAMUL/perovskite interfaces reveal that a-SAMUL exhibits stronger bidirectional adhesion to both the substrate and the buried perovskite (Supplementary Fig. 40). The origins of this enhanced interfacial adhesion are analysed by considering the distinct roles of the substrate-contacting monolayer and the buried perovskite-contacting overlayer.

For the monolayer interaction with the anode substrate, simulations of CbzNaphOH adsorbed on NiO_x reveal a standing-up conformation with lower binding energies than CbzNaph, confirming its stronger interfacial interaction (Fig. 2f). Following solvent rinsing to expose the monolayer, a-SAMUL-modified substrate exhibits higher surface coverage (Supplementary Fig. 41 and Supplementary Table 3) and molecular surface density (Supplementary Fig. 42), consistent with stronger substrate binding. For the overlayer, molecular dynamics (MD) simulations indicate strong aggregation tendencies in pristine CbzNaph, whereas incorporation of CbzNaphOH promotes a more uniform molecular distribution, as evidenced by both top-view and cross-sectional simulations (Fig. 2g). Statistical analysis of molecular tilt angles further indicates that CbzNaphOH incorporation favours a standing-up binding orientation within the overlayer (Fig. 2h).

Both SAMULs achieve full substrate coverage, as confirmed by atomic force microscopy-infrared spectroscopy measurements (Supplementary Fig. 43), with multilayer thicknesses of 6.3 nm for c-SAMUL and 12 nm for a-SAMUL determined by X-ray reflectivity (Supplementary Fig. 44). However, morphological analysis reveals a more homogeneous aggregate distribution in a-SAMUL, reflected by reduced substrate roughness and a narrower roughness distribution (Supplementary Fig. 45). Thus, although the co-SAMUL exhibits lower crystallinity than pure CbzNaph, its uniform aggregation within the film contributes to enhanced hole mobility[41] (Supplementary Fig. 46). Furthermore, the well-organized aggregate in a-SAMUL displays superior resistance to solvent erosion (Supplementary Fig. 47), effectively preventing direct contact between the perovskite layer and the anode substrate during film deposition.

Interfacial energetics

Building on the understanding of molecular packing in SAMULs, we further examined their interfacial heterogeneity and energetics. DFT calculations using a SAMUL-bound perovskite model interactions reveal that CbzNaphOH interacts more strongly with the perovskite than CbzNaph in both examined conformations (Supplementary Fig. 48), primarily due to additional interaction between the hydroxyl group in the spacer and uncoordinated Pb^{2+} ions at the perovskite surface.

https://doi.org/10.1038/s41560-026-02015-8

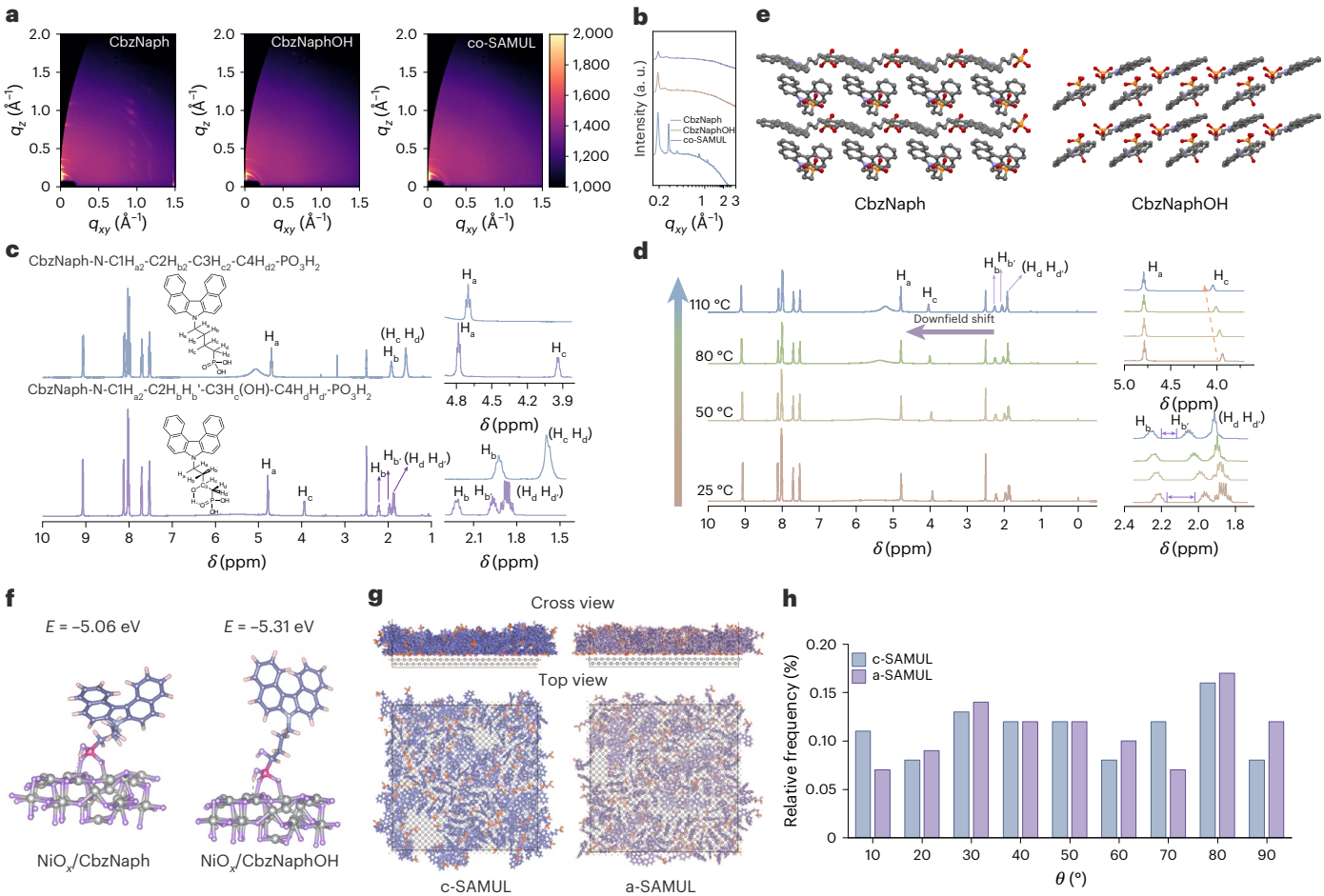

Fig. 2 | Investigation into SAMUL stacking differences arising from linker design. a, Two-dimensional GIWAXS patterns of CbzNaph, CbzNaphOH and co-SAMUL. **b**, Radial GIWAXS intensity profiles integrated over all azimuthal angles. **c**, Left: comparison of ^{1}H NMR spectra of CbzNaph and CbzNaphOH in DMSO-d_6. Arrows and boxed regions highlight characteristic spectral differences. Right: a magnified view of hydrogen-bond related spectral regions for both molecules (CbzNaph in turquoise, and CbzNaphOH in magenta). Resonances corresponding to individual protons (H_a, H_b, H_c and H_d) are labelled on the spectra. The top inset (δ 3.8–4.9 ppm) and bottom inset (δ 1.4–2.3 ppm) provide a clearer view of the chemical shift for proton pairs H_a/H_c and H_b/H_d, respectively. **d**, Variable-temperature ^{1}H NMR spectra of CbzNaphOH in DMSO-d_6, with arrows and boxed regions indicating temperature-dependent spectral evolution. The top inset (δ = 3.6–5.0 ppm) provides the temperature-dependent chemical shift evolution of the H_a and H_c, while the bottom inset (δ = 1.7–2.4 ppm) provides a clearer view of the chemical shift for the H_b and H_d protons. **e**, Simulated molecular stacking configurations of CbzNaph and CbzNaphOH molecules. **f**, DFT-calculated binding energies of SAMULs in the standing-up adsorption geometry. Atom colour coding: C(#8285B7, light violet-blue), H (#D6B5B7, light orange), N (#ADB5D8, light blue), P (#D74791, pink), O (#A491BF, lavender-grey), Ni (#97989C, grey). **g**,**h**, MD simulation showing the spatial distributions (**g**) and the tilt-angle distributions (**h**) of SAMULs on NiO$_x$ substrate.

Depth-resolved X-ray photoelectron spectroscopy of the SAMUL/buried perovskite interface shows a more gradual shift of the Pb 4*f* core-level peaks with increasing etching time for the perovskite deposited on the a-SAMUL substrate (Supplementary Fig. 49), indicating stronger and more spatially extended interfacial interactions. In addition, these enhanced buried interactions moderately improve the perovskite film quality by providing a templating effect during crystallization, as reflected in the increased crystallinity and improved morphology (Supplementary Figs. 50 and 51). Consistent trends are observed in the interfacial energetics. Compared with the c-SAMUL substrate, the perovskite layer grown on a-SAMUL substrate exhibits an energy level gradient near the interface, indicating the presence of a well-preserved overlayer aggregate that binds to the perovskite and modulates interfacial energetics (Fig. 3a,b and Supplementary Fig. 52). This energy level gradient implies a higher internal electric potential in the a-SAMUL half stack, which helps suppress minority-carrier accumulation and mitigates field-effect screening[42]. Furthermore, the interfacial energy level offset for majority carriers is reduced in a-SAMUL layer compared with the c-SAMUL layer, which is expected to contribute to a higher V_{OC} (ref. 42).

To assess the impact of interfacial energy alignment on V_{OC} and quasi-Fermi level splitting (QFLS), photoluminescence quantum yield (PLQY) measurements were conducted on both half-stack and full devices[43] (Fig. 3c). A modest improvement in QFLS was observed for the a-SAMUL half-stack (1.224 eV) compared with the c-SAMUL (1.217 eV) and NiO$_x$-only (1.205 eV) references. Transient photoluminescence measurements (Supplementary Fig. 53) further reveal a longer Shockley–Read–Hall lifetime for the a-SAMUL/perovskite half stack (2,311 ns) compared with the c-SAMUL counterpart (1,543 ns), indicating a slight reduction in both interfacial and bulk defect densities with the a-SAMUL layer. Notably, the QFLS of the full device closely matches its V_{OC}, while significant QFLS–V_{OC} mismatches are observed in the c-SAMUL device and NiO$_x$-only devices, confirming that reduced interfacial energetic offset in the a-SAMUL architecture effectively suppresses interfacial recombination.

Drift-diffusion (DD) simulations (Supplementary Tables 4 and 5) were performed to evaluate the impact of SAMUL-induced energy alignment on device performance and ionic losses, in which the simulated *J*–*V* (Fig. 3d) aligns well with the experimental data (Fig. 1j). The same

https://doi.org/10.1038/s41560-026-02015-8

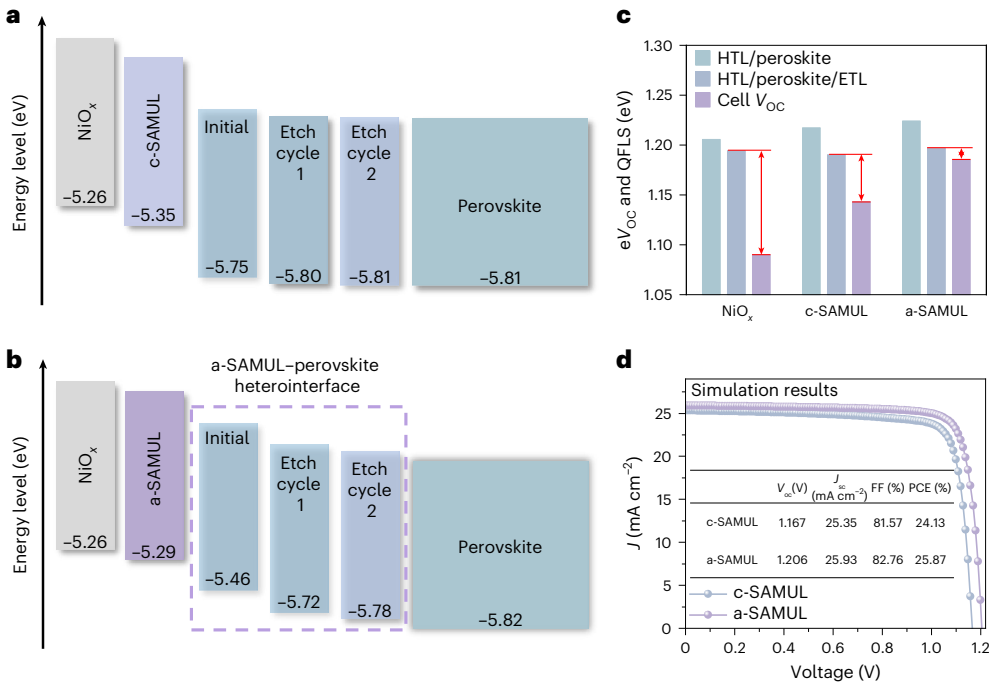

Fig. 3 | Bidirectional interfacial contact of SAMULs and corresponding interfacial energetics. a,**b**, Energy level diagrams of the buried heterointerfaces for c-SAMUL/perovskite (**a**) and a-SAMUL/perovskite (**b**). The dashed box in **b** highlights the a-SAMUL/perovskite interface. **c**, V_{OC} values obtained from J–V measurements and QFLS values derived with PLQY for half-stack device (ITO/HTL/perovskite; ITO/HTL/perovskite/ETL) and full device (ITO/HTL/perovskite/ETL/Ag). Red arrows highlight the difference between the QFLS and the device-derived effective eV_{OC}, where 'e' is the elementary charge. **d**, DD simulation of J–V characteristics for devices incorporating c-SAMUL and a-SAMUL.

simulation model reproduces the experimentally observed trends in QFLS for all partial cell stacks (Supplementary Fig. 54a) and in the FH measurements (Supplementary Fig. 54b). Notably, the simulation results indicate an exceptionally low interfacial recombination velocity at the hole-selective interface (~1 cm s^{-1}). Overall, those results confirm that a-SAMUL enhances device PCE while minimizing ionic losses. For SAMULs with full substrate coverage, both the interfacial contacts—with the anode substrate and the buried perovskite—serve as an effective barrier to ion migration. Together with favourable interfacial energetics, these features enhance device durability, with the amorphous SAMUL offering superior bidirectional molecular contact.

Stability evaluation

The stability of SAMUL-based devices was systematically evaluated under various stress conditions. Under continuous illumination (Supplementary Fig. 55) and open-circuit conditions, both devices initially exhibited stable operation; however, c-SAMUL-based devices showed substantial degradation after 300 h, as indicated by a decline in ion-freeze PCE and increased ionic losses. By contrast, in devices using the a-SAMUL, the ionic losses do not increase (Fig. 4a,b). To evaluate long-term operational and cyclic stability, devices with the optimized architecture were fabricated to isolate the effect of SAMUL selection. Under continuous maximum power point (MPP) tracking at ~45 °C under 1-sun equivalent light-emitting diode (LED) illumination, the encapsulated device retained nearly 100% of its initial PCE after 3,000 h (Fig. 4c). When the temperature was increased to 85 °C, devices incorporating a-SAMUL and c-SAMUL retained 89% and 40% of their initial PCEs after 500 and 150 h, respectively, further highlighting the superior interfacial and conformational stability afforded by the a-SAMUL interface (Supplementary Fig. 56).

Devices were then subjected to continuous reverse bias stress (−3 V) in a nitrogen-filled glovebox, with performance monitored every 10 min, which is defined as one stress cycle. Under these conditions, the c-SAMUL-based device retained only 3.0% of its initial steady-state performance after four cycles and exhibited severe ionic losses, as indicated by a pronounced decline in fill factors (Fig. 4d,e and Supplementary Fig. 57). By contrast, the device incorporating the a-SAMUL HSL retained 84.3% of its initial PCE after six cycles (Fig. 4f,g and Supplementary Fig. 58). The parallel downward shift of the PCE as a function of scan rate indicates that the performance loss under reverse bias is predominantly non-ionic in orgin[9]. When the reverse bias was reduced to −2 V, the a-SAMUL-based device maintained 93.1% of its initial PCE after 110 h, whereas the c-SAMUL-based device retained 36.7% after 60 h (Fig. 4h and Supplementary Fig. 59). This performance disparity persisted under more severe ageing conditions combining reverse bias (−2 V), illumination and elevated temperatures (85 °C), with a-SAMUL and c-SAMUL devices retaining 90% and 80% of their initial PCEs after 28 and 14 h, respectively (Supplementary Fig. 60). Consistent improvements in thermal stability were observed for devices incorporating the a-SAMUL HSL (Fig. 4i). Moreover, QFLS measurements conducted before and after thermal ageing highlight substantially smaller QFLS losses in the a-SAMUL-based stack compared with the NiO_x- and the c-SAMUL-based stacks (Supplementary Fig. 61).

Reverse bias stability improvement

Reverse bias stability was systematically studied as a function of interfacial molecular contact, SAMUL thickness and electrode selection. Using Ag electrodes, devices using c-SAMUL HSLs exhibited higher V_{rb} than those using conventional SAMs, yet still underperformed relative to a-SAMUL-based devices (V_{rb} = −4.2 V; Supplementary Fig. 62a). Incorporating a NiO_x interlayer in combination with SAM and SAMUL further improved V_{rb}. Notably, the a-SAMUL-based bilayer device achieved an improved V_{rb} of −5.6 V (Fig. 5a and Supplementary Fig. 62b). Breakdown voltage measurements as a function of SAMUL concentration revealed only minor variations once the film thickness exceeded a certain threshold, indicating that reverse bias stability is governed primarily by interfacial molecular contact rather than film thickness[9] (Supplementary Fig. 62c,d).

https://doi.org/10.1038/s41560-026-02015-8

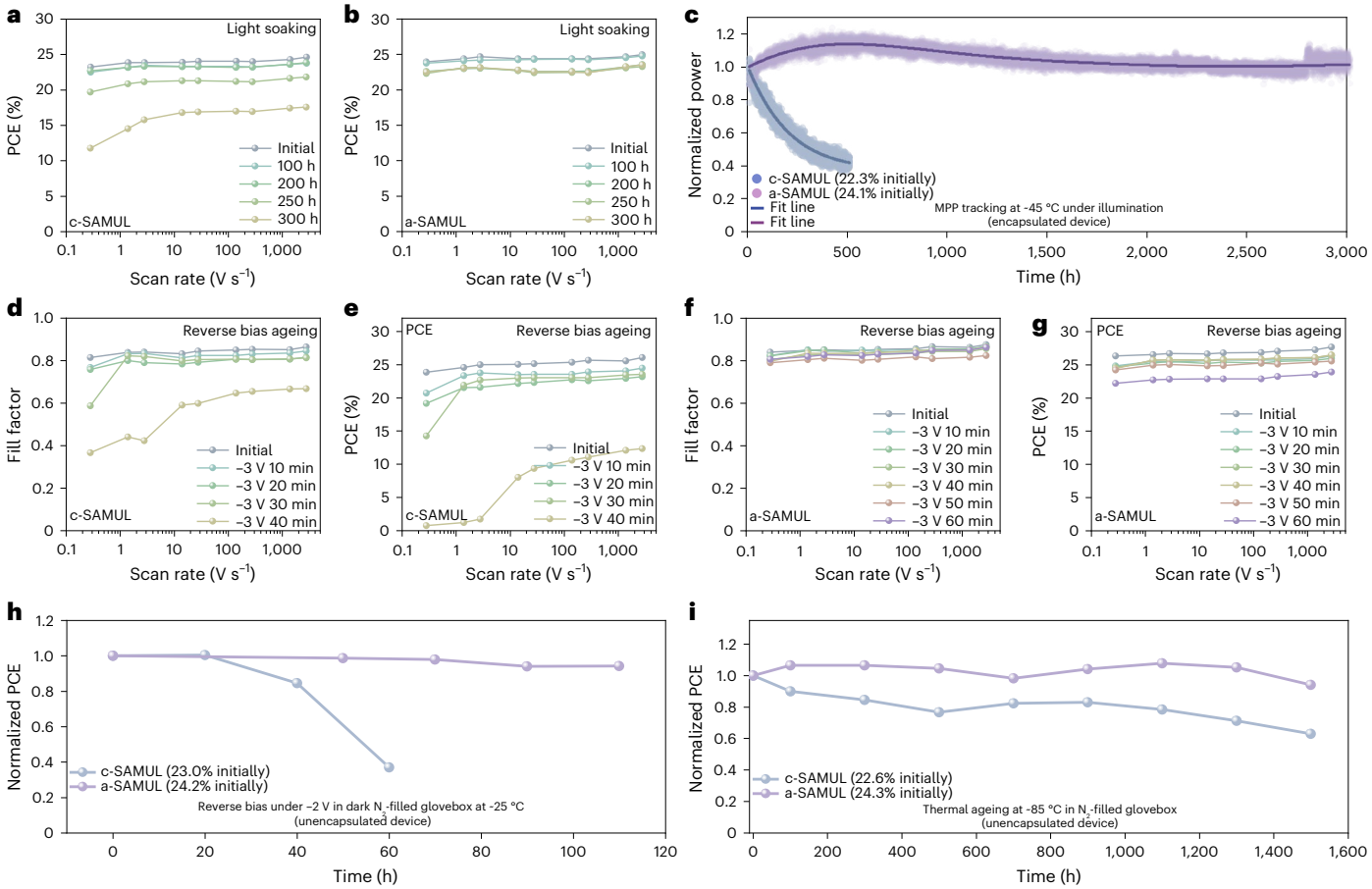

Fig. 4 | Stability assessment of the photovoltaic device. a,**b**, Ion-migration behaviours in devices incorporating c-SAMUL (**a**) and a-SAMUL (**b**) HSLs under illumination. **c**, MPP tracking of encapsulated devices under calibrated 1-sun conditions. Solid lines represent smoothed curves using adjacent averaging. **d**–**g**, Fill factor and PCE parameters extracted from FH measurements of reverse-bias-aged devices incorporating c-SAMUL (FF in **d**, and PCE in **e**) and a-SAMUL (FF in **f**, and PCE in **g**) HSLs. **h**, PCE evolution of unencapsulated devices aged under a −2 V reverse bias in a dark, N_2-filled glovebox. **i**, Intrinsic stability of unencapsulated devices aged at 85 ± 5 °C in an N_2-filled glovebox.

To determine the relationship between interfacial contact and reverse bias stability, time-of-flight secondary ion mass spectrometry (ToF-SIMS) was used. In vertically structured devices, a reverse bias of −1 V was applied for 60 s before the measurement. Significant iodide migration towards the electrode was observed in the c-SAMUL device, whereas a reduced iodide accumulation was detected for the a-SAMUL HSL (Supplementary Fig. 63). To investigate ion migration in laterally structured devices, buried perovskite films bound with SAMUL molecules were peeled from the anode substrate and integrated into a lateral architecture (channel width 200 µm), enabling in situ tracking of halide ion migration under an applied electric field. Upon gradually increasing the bias to 18 V, the c-SAMUL-bound perovskite film showed pronounced surface evolution accompanied by iodide migration towards the anode (Fig. 5c,d). By contrast, a-SAMUL-based sample showed no visible iodide migration and diffusion (Fig. 5e,f). Overlaid ion distribution maps acquired before and after bias application further emphasized these differences (Fig. 5g,h). A similar trend was observed for lead-related ion migration, although with lower intensity (Supplementary Fig. 64). These findings highlight the importance of optimized molecular contact at the HSL/perovskite heterointerface in suppressing ion migration under reverse bias.

Recent studies have demonstrated that replacing Ag with electrochemically inert Au can suppress the Ag oxidation and subsequent drift under reverse bias[9]. In such configurations, reverse bias degradation is predominantly governed by halide oxidation and lead reduction, along with field-driven migration. Beyond electrode substitution, we also investigated the impact of a SnO_x buffer layer, which expectedly provided superior reverse bias stability compared with a thinner BCP layer[44] (Supplementary Fig. 65). Consequently, a-SAMUL-based devices with an optimal electron-contact achieved an increased V_{rb} average of −17.2 V, demonstrating strong reverse bias tolerance in SAM-based HSLs and devices with PCEs exceeding 25% (Fig. 5b, Supplementary Fig. 66 and Supplementary Table 6).

To further corroborate the effectiveness of a-SAMUL in preserving perovskite integrity, mobile ion densities were quantified using bias-assisted charge extraction (BACE) measurements[45] (Fig. 5i,j). In c-SAMUL-based devices, the extracted current increased with applied bias (−3 V for 10 min), indicating elevated mobile ion densities and accelerated degradation under strong electric fields. By contrast, a-SAMUL-based devices exhibited minimal variation in extracted charge across the bias range, confirming robust interfacial heterogeneity and strong resistance to ion migration. The clear correlation between ionic loss and reverse bias tolerance (Fig. 5k) further validates that suppression of ion migration is a key determinant of enhanced reverse bias stability.

Conclusion

In this work, we establish a comprehensive correlation between the structural optimization of SAM-based HSLs—including SAM only, c-SAMUL and a-SAMUL architectures—and ion migration-driven instability in PSCs. During film formation, conventional SAMs with

https://doi.org/10.1038/s41560-026-02015-8

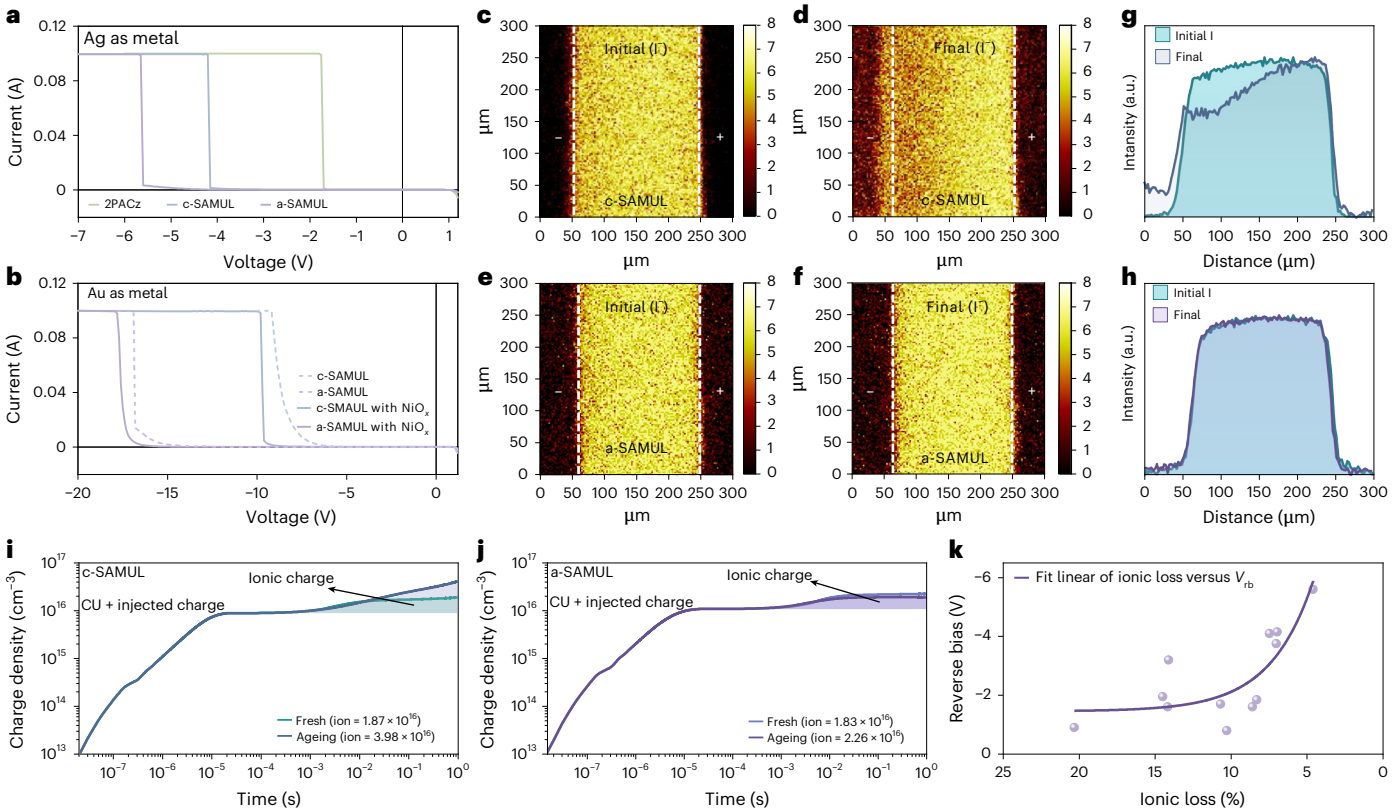

Fig. 5 | Analysis of mobile ion migration under reverse bias conditions. **a**, Dark*J*–*V* curves illustrating reverse bias performance of devices (0.0875 cm^2) using different SAMs/SAMULs with Ag as metal. **b**, Dark*J*–*V* curves illustrating the reverse bias performance of devices (0.0875 cm^2) using different SAMULs with Au as electrodes. **c**–**h**, ToF-SIMS ion mapping (**c**–**f**) and corresponding integrated depth profiles (c-SAMUL in **g** and a-SAMUL in **h**) acquired before (c-SAMUL in **c** and a-SAMUL in **e**) and after (c-SAMUL in **d** and a-SAMUL in **f**) application of a constant 18 V bias to devices based on c-SAMUL and a-SAMUL. **i**,**j**, Integrated mobile charge density extracted from the current transients in BACE measurements of c-SAMUL-based (**i**) and a-SAMUL-based (**j**) devices before and after a −3 V bias for 10 min. The ionic contribution is highlighted by shaded regions and arrows. CU denotes the electrode charge. **k**, Relationship between measured ionic loss and reverse bias tolerance. The solid line represents a mono-exponential fit.

limited π-conjugation form ultrathin and inhomogeneously packed interfacial layers, resulting in incomplete molecular contact with the buried perovskite. Incorporation of a π-extended unit in c-SAMUL improves charge transport across the overlayer; however, its flexible linker promotes excessive aggregation, leading to spatially non-uniform packing and weakened perovskite interfacial contact. By contrast, introducing a hydroxyl group into the c-SAMUL linker induces intramolecular non-covalent interactions that alter molecular stacking, yielding a uniformly aggregated, amorphous SAMUL. With respect to reverse bias stability, a-SAMUL forms a dense and conformally stable interlayer that acts both as a physical barrier suppressing leakage currents and as a bidirectionally optimized molecular contact that stabilizes the heterointerface and the buried perovskite surface. This dual role effectively suppresses the creation of mobile ions under reverse bias. Furthermore, a-SAMUL enables a higher hole mobility through homogenous film aggregation and a favourable interfacial energy alignment compared with c-SAMUL, thereby maximizing the V_{OC}. The optimized a-SAMUL/perovskite interface achieved a certified PCE of 26.3% while limiting ion-induced performance losses to 5.7%. When integrated into optimal device architecture, this engineered hole-selective interface enabled an average breakdown voltage exceeding −17 V, surpassing that of conventional SAM-based devices. These findings highlight the importance of heterogeneity engineering at buried interfaces and demonstrate the potential of applying SAMUL architectures to simultaneously achieve high efficiency, long-term operational stability and large reverse breakdown voltages in PSCs.

Methods

All the chemical reagents were purchased and used as received unless otherwise indicated. All air- and water-sensitive reactions were performed under a nitrogen atmosphere. Dichloromethane (99.99%, J&K), chloroform ($CHCl_3$, 99.99%, J&K), tetrahydrofuran (99.99%, J&K), toluene (99.99%, J&K) and *N*,*N*-dimethylformamide (DMF, 99.99%, J&K) were dried by a JC Meyer solvent drying system before use. DMSO (99.70%, J&K), isopropanol (IPA, 99.50%, J&K) and chlorobenzene (CB, 99.90%, Sigma) were sourced from J&K. CsI, MAI, MACl, MABr, $EDAI_2$, 4F-PEAI, C_{60} and BCP were obtained from Xi'an Polymer Light Technology. PbI_2 (99.9985%), $PbBr_2$, 2PACz, 4PACz, Me-4PACz and CbzNaph were procured from TCI. Formamidine hydroiodide (FAI) was sourced from Dysol. Nickel oxide nanoparticles (NiO_x, >99.999%) were purchased from Advanced Election Technology.

Synthesis of CbzNaphOH

The synthetic routes are shown in Supplementary Information, scheme 1.

For the synthesis of compound 2 (4-(7*H*-dibenzo[c,g]carbazol-7-yl) butyl oxirane), compound 1 (7*H*-dibenzo[c,g]carbazole, 300 mg, 1.12 mmol) and potassium hydroxide (145 mg, 2.58 mmol) were dissolved in degassed DMF (7 ml) under a nitrogen atmosphere. The mixture was stirred at 0 °C for 30 min, after which (2-bromoethyl) oxirane (695 mg, 4.60 mmol) was added. The reaction was allowed to proceed at room temperature for 16 h. Upon completion, the reaction mixture was quenched with water and extracted with ethyl acetate. The combined extracts were washed with brine, dried over anhydrous

sodium sulfate and concentrated under reduced pressure. The crude product was purified by silica gel column chromatography using hexane/CH_2Cl_2 (v/v = 2:1) as the eluent to afford compound 2 as a colourless viscous liquid (316 mg, 83.5%). ^{1}H NMR (400 MHz, $CDCl_3$): δ = 9.33–9.16 (d, J = 8.4 Hz, 2H, Ph-*H*), 8.11–8.03 (d, J = 8.0 Hz, 2H, Ph-*H*), 7.96–7.87 (d, J = 8.8 Hz, 2H, Ph-*H*), 7.79–7.66 (m, 4H, Ph-*H*), 7.60–7.50 (m, 2H, Ph-*H*), 4.79–4.56 (m, 2H, CH_2), 2.88–2.78 (m, 1H, CH_2), 2.70–2.61 (t, J = 4.4 Hz, 1H, CH_2), 2.40–2.34 (m, 1H, CH_2), 2.34–2.23 (m, 1H, CH_2), 1.95–1.82 (m, 1H, CH_2). ^{13}C NMR (100 MHz, $CDCl_3$): δ = 136.83, 129.69, 129.12, 129.09, 126.65, 125.40, 125.04, 123.23, 117.28, 110.53, 77.32, 77.00, 76.68, 49.71, 47.32, 39.90, 32.92.

For the synthesis of compound 3 (diethyl (4-(7*H*-dibenzo[*c*,*g*]carbazol-7-yl)-3-hydroxybutyl)phosphonate), compound 2 (316 mg, 0.94 mmol) and triethyl phosphite (163 mg, 1.22 mmol) were dissolved in degassed toluene (10 ml) under a nitrogen atmosphere and stirred at room temperature for 30 min. Zinc chloride (128 mg, 0.94 mmol) was then added, and the reaction mixture was heated to 60 °C and stirred for 12 h. After cooling to room temperature, the reaction was quenched with water and extracted with ethyl acetate. The combined extracts were washed with brine, dried over anhydrous $NaSO_4$ and concentrated under reduced pressure. The crude product was purified by silica gel column chromatography using ethyl acetate/CH_2Cl_2 (v/v = 1:2) as the eluent to afford compound 3 as a colourless viscous liquid (290 mg, 65.1%). ^{1}H NMR (400 MHz, $CDCl_3$): δ = 9.28–9.14 (d, J = 8.4 Hz, 2H, Ph-H), 8.10–8.00 (d, J = 8.0 Hz, 2H, Ph-H), 7.96–7.88 (d, J = 8.8 Hz, 2H, Ph-H), 7.87–7.80 (d, J = 8.8 Hz, 2H, Ph-H), 7.74–7.63 (t, J = 7.6 Hz, 2H, Ph-H), 7.57–7.48 (t, J = 7.6 Hz, 2H, Ph-H), 4.91–4.62 (m, 2H, N-CH_2), 4.05–3.88 (m, 5H, CHOH, P(O)(OCH_2CH_3)), 2.18–2.02 (m, 2H, N-CH_2CH_2), 1.89–1.71 (m, 2H, CH_2P), 1.26–1.18 (t, J = 7.2 Hz, 3H, P(O)(OCH_2CH_3)), 1.13–1.04 (t, J = 7.2 Hz, 3H, P(O)(OCH_2CH_3)). ^{13}C NMR (100 MHz, $CDCl_3$): δ = 136.95, 129.58, 129.03, 128.98, 126.43, 125.22, 124.90, 123.03, 117.05, 110.83, (63.53, 63.48, d, $^2J_{C,P}$ = 5 Hz, CHOH), (61.93, 61.86, 61.79, t, $^2J_{C,P}$ = 7.2 Hz, P(O)(OCH_2CH_3)$_2$), (39.22, 39.20, d, $^4J_{C,P}$ = 2 Hz, NCH_2), (38.02, 37.86, d, $^3J_{C,P}$ = 16.5 Hz, P(O)(OCH_2CH_3)$_2$), (34.13, 32.76, d, $^1J_{C,P}$ = 137.1 Hz, CH_2P), (16.16, 16.10, d, $^3J_{C,P}$ = 5.9 Hz), (16.07, 16.01, $^3J_{C,P}$ = 5.8 Hz).

For the synthesis of compound 4 ((4-(7*H*-dibenzo[c,g]carbazol-7-yl)-3-hydroxybutyl)phosphonic acid), compound 3 (290 mg, 0.61 mmol) was dissolved in degassed dichloromethane (10 ml) under a nitrogen atmosphere. Bromotrimethylsilane (15 equiv., 1.40 g, 1.17 ml, 9.15 mmol) was added dropwise, and the reaction mixture was stirred at room temperature for 12 h. After completion, the solvent was partially removed under reduced pressure. The resulting residue was dissolved in 5 ml ethanol, followed by dropwise addition of distilled water (10 ml) until the solution became opaque. The precipitated product was collected by filtration and washed thoroughly with water to afford compound 4 as a white solid (176 mg, 68.8%). ^{1}H NMR (400 MHz, DMSO-d_6): δ = 9.13–9.00 (d, J = 8.4 Hz, 2H, Ph-H), 8.18–8.09 (d, J = 8.0 Hz, 2H, Ph-H), 8.08–7.92 (d, J = 8.8 Hz, 2H, Ph-H), 7.87–7.80 (q, J = 8.8 Hz, 4H, Ph-H), 7.76–7.65 (t, J = 7.2 Hz, 2H, Ph-H), 7.57–7.47 (t, J = 7.2 Hz, 2H, Ph-H), 4.82–4.74 (t, J = 7.2 Hz, 2H, N-CH_2), 4.00–3.86 (m, 1H, CHOH), 2.27–2.16 (m, 1H, N-CH_2CHH), 2.02–1.92 (m, 1H, N-CH_2CHH), 1.92–1.81 (m, 2H, CH_2P). ^{13}C NMR (100 MHz, DMSO-d_6): δ = 136.85, 129.37, 129.26, 128.44, 126.44, 125.52, 124.16, 123.12, 115.93, 111.75, 63.81, (37.42, 37.34, d, $^3J_{C,P}$ = 7.6 Hz, NCH_2CH_2), (36.92, 35.61, d, $^1J_{C,P}$ = 130.5 Hz, CH_2P).

Precursor preparation

To prepare the 1.55-eV triple cation perovskite, 1.6 M perovskite precursor solutions were formulated by mixing FAI, MAI, PbI_2 and CsI in DMF:DMSO solvent (volume ratio 4:1) with the chemical formula $Cs_{0.05}FA_{0.85}MA_{0.1}PbI_3$. Excessive 5% PbI_2, 12% MACl and 1.6 mg of 4F-PEAI additives were added to the precursor solution, and no filtration was required before use.

To prepare 1.68-eV-bandgap perovskite, 1.4 M perovskite precursor solutions were formulated by mixing FAI, MAI, $PbBr_2$, PbI_2 and CsI in DMF:DMSO solvent (volume ratio 4:1) with the chemical formula $Cs_{0.05}FA_{0.8}MA_{0.15}Pb(I_{0.75}Br_{0.25})_3$. Excessive 5% PbI_2, 5% MABr additives were added to the precursor solution, and no filtration was required before use.

To prepare the double cation FACs-based perovskite, 1.5 M perovskite precursor solutions were formulated by mixing FAI, PbI_2 and CsI in DMF:DMSO solvent (volume ratio 4:1) with the chemical formula $Cs_{0.05}FA_{0.95}PbI_3$. Excessive 5% PbI_2, 12% MACl and 1.6 mg of 4F-PEAI additives were added to the precursor solution, and no filtration was required before use.

Device fabrication

The prepatterned ITO glass substrates underwent thorough cleaning by sonication with a detergent, deionized water, acetone and IPA successively, each for 30 min. Subsequently, the cleaned ITO glass substrates were dried in an oven at 80 °C for 24 h and treated with O_2 plasma for 30 min before use. Different hole-contact layers were prepared as follows. NiO_x (20 mg ml^{-1} in pure water) was spin-coated onto the ITO glass substrates at 2,000 rpm for 30 s and subsequently annealed at 150 °C for 30 min. PTAA was dissolved in chlorobenzene (CB) solvent at a concentration of 1.5 mg ml^{-1}. The 2PACz, 4PACz, Me-4PACz and CbzNaph hole-selective SAMs (stock solutions 100 mg ml^{-1} in DMF) were diluted with ethanol to the desired concentrations. The CbzNaphOH (100 mg ml^{-1} in DMF) was diluted with ethanol to the required concentration. Co-SAMUL solutions were prepared by mixing CbzNaph and CbzNaphOH in ethanol at the desired ratios. The resulting solution was spin-coated onto the ITO glass substrates at 3,000 rpm for 30 s and subsequently annealed at 100 °C for 10 min. For the NiO_x-combined SAMs or SAMULs, the corresponding solutions were directly deposited onto the preformed NiO_x substrates. The SAMs were rinsed by dropping 200 µl ethanol onto the film while spinning at 3,000 rpm, followed by annealing at 100 °C for 10 min. By contrast, no solvent rinsing was performed for the prepared SAMUL substrates.

Next, for the $Cs_{0.05}FA_{0.85}MA_{0.1}PbI_3$ triple cation perovskite, 40 µl of the perovskite precursor was spin-coated at 5,000 rpm for 30 s, with 180 µl of CB antisolvent added to the centre of the wetted film 5 s before the end of the process. For the $Cs_{0.05}FA_{0.8}MA_{0.15}Pb(I_{0.75}Br_{0.25})_3$ triple cation perovskite, 40 µl of the perovskite precursor was spin-coated at 4,000 rpm for 30 s, with 180 µl of CB antisolvent added to the centre of the wetted film 5 s before the end of the process. For the $Cs_{0.05}FA_{0.95}PbI_3$ double cation perovskite, 40 µl of the perovskite precursor was spin-coated at 5,000 rpm for 30 s, with 180 µl of CB antisolvent added to the centre of the wetted film 5 s before the end of the process. Those wetted films were annealed at 100 °C for 30 min. Subsequently, $EDAI_2$ solution (0.4 mg ml^{-1} in IPA) was spin-coated onto the formed perovskite at 3,000 rpm for 30 s and annealed at 100 °C for 10 min. Then, 20-nm C_{60}, 5-nm BCP (or 20-nm SnO_x was deposited by atomic layer deposition) and 90-nm Ag (or 60-nm Au) were thermally evaporated in a high-vacuum chamber (<1×10^{-4} torr).

Device characterizations

The J–V characteristics of devices were measured in a N_2-filled glovebox using a Keithley 2400 Source Meter under simulated sunlight from a solar simulator. To achieve an AM 1.5 G (100 mW cm^{-2}) solar simulator light intensity, a National Renewable Energy Laboratory-calibrated silicon solar cell (with a KG-2 filter) was used. A shadow mask with an aperture area of 0.068 cm^2 (unmasked 0.0875 cm^2) was used for J–V measurements. We used scan speeds of 200 and 500 mV s^{-1} for the light and wider-range reverse J–V measurements, respectively. The breakdown voltage (V_{rb}) was defined at the point at which the current starts to rise when scanning and plotting the current to the set compliance limit of the Keithley of 0.1 A. We note that this method gives a V_{rb} nearly identical to that obtained by fitting a straight line in the region before the reverse maximum power current density (for example, −15 to −25 mA cm^{-2}) and taking the interception with the x axis (y = 0) as suggested earlier[9]. For reverse bias stability measurements, the devices

were subjected to a reverse bias using an RST3000 electrochemical workstation inside an N_2-filled glovebox, either at room temperature in the dark or on an 85 °C hot plate under LED illumination.

Stability tests of solar cells

The operational stability of the encapsulated devices outside a glovebox was measured by a commercial multichannel stability test system (Wuhan 91PVKSolar) in MPP tracking mode, either at room temperature or 85 °C hot plate. The illumination was achieved by a 1-sun-equivalent white-light LED (spectrum provided in Supplementary Fig. 55), and the light intensity was calibrated to achieve the same J_{SC} from the devices measured under a standard solar simulator (AM 1.5 G, 100 mW cm^{-2}). For long-term operational and cyclic stability testing, the optimized device configuration (ITO/NiO_x/SAMUL/perovskite/C_{60}/SnO_x/Au) was used.

FH measurements

Fast J–V curves were obtained by applying a triangular voltage pulse to the cells starting from approximately open circuit (V_{OC}), followed by a reverse sweep from V_{OC} to −0.1 V and a forward sweep from −0.1 V to V_{OC} with variable frequency or scan speed (V s^{-1}) using the FastChar setup from SolarSense Technologies. The duration of the hold voltage at V_{OC} was five times longer than the total scan time of the voltage sweep. The voltage response of the cell was measured with an oscilloscope, using an external load resistance of 2–5 Ω, and the voltage pulse was supplied by a function generator. Despite the different hardware and measurement routines, the testing conditions were the same as those used for the standard J–V measurements as described above. We note that, to cross-check the FH results at slow scan speeds (100–300 mV s^{-1}), standard J–V measurements were performed on the same cells, which resulted in a nearly identical performance metric as obtained with the FH setup.

BACE

BACE measurements were performed using the FastChar set-up from SolarSense Technologies. In this measurement, the device was initially held at a voltage close to the open-circuit voltage, where the injected charge equals the short-circuit current. After a preset delay time, a bias of 0 V was applied to extract the injected and capacitive charge in the device at short times (μs), and mobile ions on long times (s). The delay times for the fresh devices were chosen to be typically five times longer than the extraction time of charges observed under the collection bias (typically ~5–10 s) to allow ionic charges to distribute throughout the active layer. Short-time transients in the millisecond range were recorded with a rather low load resistance (for example, 500 Ω), while long-time transients in the second range were measured with a large resistance (for example, 50,000 Ω) to enable resolution of low ionic drift currents. We ensured that the oscilloscope offset current at the given load resistance was significantly lower than the measured extraction current.

DFT calculations

The electron density distributions are calculated using the DFT method with the software of CP2K v2024.1 program utilizing a DZVP-MOLOPT-SR-GTH basis and the Perdew–Burke–Ernzerhof exchange-correlation functional[46,47]. The non-covalent interaction is systematically computed to characterize the spatial distribution of non-covalent bonding interactions within the system. All calculations were performed within the framework of DFT calculation, with wavefunction data extracted from self-consistent field converged charge densities. The data post-processing and visualization were performed using the Multiwfn 3.8 and VMD (Visual Molecular Dynamics) 1.9.4 packages, respectively[48–50].

The adsorption energies of c-SAMUL or a-SAMUL on the NiO_x surfaces were calculated on the basis of the generalized gradient approximation with the Perdew–Burke–Ernzerhof exchange-correlation functional using the CASTEP module implementation[51,52]. The lattice parameters and atomic coordinates were fully optimized until convergence to obtain the ground-state electronic structure. A vacuum layer of 20 Å was introduced along the z-direction to eliminate spurious interactions between periodic images. A plane-wave basis set with an energy cut-off of 450 eV was used to describe the valence electrons, and the Tkatchenko–Scheffler dispersion correction was included to accurately account for long-range van der Waals interactions[53,54]. The convergence criteria were set such that the residual force on each atom was less than 0.02 eV Å^{-1}, and the total energy change between successive iterations was below 1×10^{-5} eV per atom. The adsorption energy (E_{ads}) was calculated according to the following equation[55]:

$$E_{ads} = E_{complex} - \Delta E_{SAMUL} - E_{surface},$$

where $E_{complex}$ is the total energy of the c-SAMUL or a-SAMUL-surface complex, ΔE_{SAMUL} is the energy of c-SAMUL or a-SAMUL, and $E_{surface}$ is the total energy of the NiO surface.

MD calculations

All MD simulations were carried out using LAMMPS and were based on the Universal Force Field[56,57]. The Verlet integrator was used with a time step of 1 fs, and the Nosé–Hoover thermostat was employed for temperature control[58,59]. A 12.5 Å cut-off was used for both van der Waals and the real-space part of electrostatics, with long-range electrostatics treated using the particle–particle particle–mesh (PPPM) method[60]. To evaluate the orientation of c-SAMUL or a-SAMUL molecules by themselves, we built two rectangular NiO (100) surfaces with a size of 71.1 Å × 71.1 Å. Then, a 50 Å vacuum was added along the direction normal to the substrate. The system was first equilibrated under the NPT ensemble (298.15 K, 1.01325 bar) for 0.5 ns, followed by an additional 0.5 ns of NVT equilibration at 298.15 K. Subsequently, production MD simulations were performed for 5 ns in the NVT ensemble.

SETFOS simulations

DD simulations were performed using the commercially available software SETFOS 5.5.10 from FLUXiM. SETFOS numerically solves a system of three coupled equations, namely the Poisson equation, the continuity equation and the DD equation. The Poisson equation is given by

$$\frac{\partial^2 \varphi(x)}{\partial x^2} = -\frac{q}{\varepsilon}(p(x) - n(x) + c(x) - a(x) + N_D^+ - N_A^-),$$

where $\varphi(x)$, $p(x)$, $n(x)$, $c(x)$ and $a(x)$ denote electrical potential, hole density, electron density, cation density and anion density at each position respectively, N_D^+ and N_A^- are the donor and acceptor density, q is the electron charge and ε is the absolute permittivity of the material. The continuity equations for the electrons and holes are given by

$$\frac{\partial n}{\partial t} = -\frac{1}{q}\frac{\partial J_n}{\partial x} - R(x) + G(x)$$

$$\frac{\partial p}{\partial t} = -\frac{1}{q}\frac{\partial J_p}{\partial x} - R(x) + G(x),$$

where J_n and J_p are the electron and hole current density, and $R(x)$ and $G(x)$ are the recombination and generation rate, respectively. The DD equations are given by

$$J_n = qn(x)\mu_n\frac{\partial \varphi}{\partial x} + qD_n\frac{\partial n(x)}{\partial x}$$

$$J_p = qp(x)\mu_p\frac{\partial \varphi}{\partial x} + qD_p\frac{\partial p(x)}{\partial x},$$

where μ_n and μ_p are the mobilities of electrons and holes, and D_n and D_p are the diffusion constants of electrons and holes. Continuity equations and DD equations also apply to mobile ions. The mobility and the diffusion constants are related via the Einstein relation

$$D = \frac{\mu k_B T}{q},$$

where k_B is the Boltzmann constant and T is the temperature. The relationship between minority and majority carrier concentrations at equilibrium obeys the following equations:

$$n_0(x)\,p_0(x) = n_i^2 = N_C N_V \exp\left(\frac{-E_g}{k_B T}\right),$$

where n_0 and p_0 are electron and hole densities at equilibrium, n_i is the intrinsic carrier concentration, E_g is the bandgap, and N_C and N_V are effective densities of state. While under illumination, the following equations apply

$$n(x)\,p(x) = N_C N_V \exp\left(\frac{-E_g}{k_B T}\right)\exp\left(\frac{E_{F,n} - E_{F,p}}{k_B T}\right)$$

$$n(x) = N_C \exp\left(\frac{E_{F,n} - E_c}{k_B T}\right)$$

$$p(x) = N_V \exp\left(\frac{E_V - E_{F,p}}{k_B T}\right),$$

where $E_{F,n}$ and $E_{F,p}$ are quasi-Fermi energy levels of electrons and holes, respectively. The recombination in the bulk material is given by the following equations:

$$R(x) = R_{SRH} + R_{radiative}$$

$$R_{radiative}(x) = k_2(n(x)\,p(x) - n_i^2)$$

$$R_{SRH}(x) = \frac{n(x)\,p(x) - n_i^2}{(n(x) + n_1)\,\tau_p + (p(x) + p_1)\,\tau_n},$$

where k_2 is the radiative radiation coefficient, τ_p and τ_n are the minimum Shockley-Read-Hall (SRH) lifetimes for holes and electrons, $n_1 = N_C \exp(\frac{E_T - E_c}{k_B T})$, $n_2 = N_V \exp(\frac{E_V - E_T}{k_B T})$, and E_T is the energy level of traps. The minimum SRH lifetime in the bulk is given by

$$\tau_{p/n} = \frac{1}{N_t \upsilon_{th} \sigma},$$

where N_t is the trap density, $\upsilon_{th} = \sqrt{\frac{3k_B T}{m^*}}$ and m^* are the thermal velocity and the effective mass of charge carriers, respectively, and σ is the cross-section of traps. The generation is given by

$$G(x) = \int_{\lambda_{min}}^{\lambda_{max}} \alpha(\lambda)\, N_{phot}(\lambda, x)\mathrm{d}\lambda,$$

where α is the wavelength-dependent absorptivity, which we determined experimentally, and N_{phot} is the photon flux at each position, which is calculated through the generalized matrix method.

Other characterizations

^{1}H NMR and ^{13}C NMR spectra were recorded on Bruker ARX-400 (400 MHz). Allchemical shifts were reported in parts per million (ppm). ^{1}H NMR chemical shifts were referenced to $CDCl_3$ (7.26 ppm), and ^{13}C NMR chemical shifts were referenced to $CDCl_3$ (77.00 ppm). The morphology of the film samples was examined using SEM (QUATTRO S). The thickness of the film was examined by Bruker Dektak XT stylus profilometer and X-ray reflectivity measurement test by Rigaku Smartlab. Powder and thin-film XRD characterizations were conducted using a D2 Phaser instrument with Cu Kα radiation (wavelength of 1.5418 Å). X-ray photoelectron spectroscopy analysis was conducted using a Thermo Fisher ESCALAB Xi+ X-ray photoelectron spectrometer. Cyclic voltammetry measurements were conducted using a CHI1020D electrochemical workstation. Ultraviolet light from a non-monochromatic He I source with an energy of 21.21 eV was utilized for the measurement. Time-resolved photoluminescence was recorded using an FLS980 spectrofluorometer (Edinburgh) with a 485-nm pulsed excitation laser, peak power of 115.19–222.22 mW and beam size of 1.5 mm^2. A low repetition rate was used ($1/f >$ lifetime, ~100 kHz), as well as a low fluence ~10 nJ cm^{-2}. ToF-SIMS measurements were performed on a PHI nanoToFII. For sputtering, pulsed primary ions from an O_2 liquid metal ion gun (1 keV) were employed, while analysis was carried out using a pulsed primary ion beam of Bi^{3+} (30 keV). Atomic force microscopy images were obtained using an Oxford Instruments Asylum Research Cypher ES. GIWAXS was carried out at the BL14B1 beamline of the Shanghai Synchrotron Radiation Facility. The film's adhesion strength was tested by CMT 5105.

Reporting summary

Further information on research design is available in the Nature Portfolio Reporting Summary linked to this article.

Data availability

All data generated or analysed during this study are included in the Article and its Supplementary Information. Source data are provided with this paper.

References

1. Zhang, X. et al. Advances in inverted perovskite solar cells. *Nat. Photonics* **18**, 1243–1253 (2024).
2. Liu, C. et al. Bimolecularly passivated interface enables efficient and stable inverted perovskite solar cells. *Science* **382**, 810–815 (2023).
3. Li, M., Liu, M., Qi, F., Lin, F. R. & Jen, A. K. Self-assembled monolayers for interfacial engineering in solution-processed thin-film electronic devices: Design, fabrication, and applications. *Chem. Rev.* **124**, 2138–2204 (2024).
4. Khenkin, M. V. et al. Consensus statement for stability assessment and reporting for perovskite photovoltaics based on ISOS procedures. *Nat. Energy* **5**, 35–49 (2020).
5. Wu, S. et al. Redox mediator-stabilized wide-bandgap perovskites for monolithic perovskite-organic tandem solar cells. *Nat. Energy* **9**, 411–421 (2024).
6. Mariani, P. et al. Low-temperature strain-free encapsulation for perovskite solar cells and modules passing multifaceted accelerated ageing tests. *Nat. Commun.* **15**, 4552 (2024).
7. Ummadisingu, A. et al. The effect of illumination on the formation of metal halide perovskite films. *Nature* **545**, 208–212 (2017).
8. Wang, W.-T. et al. Water- and heat-activated dynamic passivation for perovskite photovoltaics. *Nature* **632**, 294–300 (2024).
9. Jiang, F. et al. Improved reverse bias stability in p–i–n perovskite solar cells with optimized hole transport materials and less reactive electrodes. *Nat. Energy* **9**, 1275–1284 (2024).
10. Diethelm, M. et al. Probing ionic conductivity and electric field screening in perovskite solar cells: a novel exploration through ion drift currents. *Energy Environ. Sci.* **18**, 1385–1397 (2025).
11. Wang, X. et al. Regulating phase homogeneity by self-assembled molecules for enhanced efficiency and stability of inverted perovskite solar cells. *Nat. Photonics* **18**, 1269–1275 (2024).

12. Yuan, Y. & Huang, J. Ion migration in organometal trihalide perovskite and its impact on photovoltaic efficiency and stability. *Acc. Chem. Res.* **49**, 286–293 (2016).
13. Chen, R. et al. Rear electrode materials for perovskite solar cells. *Adv. Funct. Mater.* **32**, 2200651 (2022).
14. Zhu, H. et al. Long-term operating stability in perovskite photovoltaics. *Nat. Rev. Mater.* **8**, 569–586 (2023).
15. Calado, P. et al. Evidence for ion migration in hybrid perovskite solar cells with minimal hysteresis. *Nat. Commun.* **7**, 13831 (2016).
16. Li, N. et al. Barrier reinforcement for enhanced perovskite solar cell stability under reverse bias. *Nat. Energy* **9**, 1264–1274 (2024).
17. Ni, Z. et al. Evolution of defects during the degradation of metal halide perovskite solar cells under reverse bias and illumination. *Nat. Energy* **7**, 65–73 (2021).
18. Xu, Z. et al. Halogen redox shuttle explains voltage-induced halide redistribution in mixed-halide perovskite devices. *ACS Energy Lett.* **8**, 513–520 (2022).
19. Kirmani, A. R. et al. Metal oxide barrier layers for terrestrial and space perovskite photovoltaics. *Nat. Energy* **8**, 191–202 (2023).
20. Huang, X. et al. Polyoxometalate reinforced perovskite phase for high-performance perovskite photovoltaics. *Adv. Mater.* **36**, e2410564 (2024).
21. Liu, J. et al. Efficient and stable perovskite-silicon tandem solar cells through contact displacement by MgF_x. *Science* **377**, 302–306 (2022).
22. Ren, X. et al. Mobile iodides capture for highly photolysis- and reverse-bias-stable perovskite solar cells. *Nat. Mater.* **23**, 810–817 (2024).
23. Wu, W. et al. Stable and uniform self-assembled organic diradical molecules for perovskite photovoltaics. *Science* **389**, 195–199 (2025).
24. Liu, S. et al. Buried interface molecular hybrid for inverted perovskite solar cells. *Nature* **632**, 536–542 (2024).
25. Di Girolamo, D. et al. Silicon / perovskite tandem solar cells with reverse bias stability down to −40 V. Unveiling the role of electrical and optical design. *Adv. Sci.* **11**, e2401175 (2024).
26. Li, R., Gong, R., Lin, H., Green, M. A. & Lan, D. Reverse-bias challenges facing perovskite–silicon tandem solar cells under field conditions. *Newton* **1**, 100001 (2025).
27. Bertoluzzi, L. et al. Incorporating electrochemical halide oxidation into drift-diffusion models to explain performance losses in perovskite solar cells under prolonged reverse bias. *Adv. Energy Mater.* **11**, 2002027 (2021).
28. Thiesbrummel, J. et al. Ion-induced field screening as a dominant factor in perovskite solar cell operational stability. *Nat. Energy* **9**, 664–676 (2024).
29. Le Corre, V. M. et al. Quantification of efficiency losses due to mobile ions in perovskite solar cells via fast hysteresis measurements. *Sol. RRL* **6**, 2100772 (2022).
30. Li, D. et al. Co-adsorbed self-assembled monolayer enables high-performance perovskite and organic solar cells. *Nat. Commun.* **15**, 7605 (2024).
31. Xiong, W. et al. Controllable p- and n-type behaviours in emissive perovskite semiconductors. *Nature* **633**, 344–350 (2024).
32. He, R. et al. Improving interface quality for 1-cm^2 all-perovskite tandem solar cells. *Nature* **618**, 80–86 (2023).
33. Tockhorn, P. et al. Nano-optical designs for high-efficiency monolithic perovskite–silicon tandem solar cells. *Nat. Nanotechnol.* **17**, 1214–1221 (2022).
34. Jiang, W. et al. π-expanded carbazoles as hole-selective self-assembled monolayers for high-performance perovskite solar cells. *Angew. Chem. Int. Ed* **134**, e202213560 (2022).
35. Jiang, W. et al. Spin-coated and vacuum-processed hole-extracting self-assembled multilayers with h-aggregation for high-performance inverted perovskite solar cells. *Angew. Chem. Int. Ed* **63**, e202411730 (2024).
36. Yu, S. et al. Homogenized NiO_x nanoparticles for improved hole transport in inverted perovskite solar cells. *Science* **382**, 1399–1404 (2023).
37. Li, Z. et al. Stabilized hole-selective layer for high-performance inverted p–i–n perovskite solar cells. *Science* **382**, 284–289 (2023).
38. Ding, J., Rahman, O. U., Peng, W., Dou, H. & Yu, H. A novel hydroxyl epoxy phosphate monomer enhancing the anticorrosive performance of waterborne graphene/epoxy coatings. *Appl. Surf. Sci.* **427**, 981–991 (2018).
39. Luo, Y. et al. Understanding and measurement for the binding energy of hydrogen bonds of biomass-derived hydroxyl compounds. *J. Phys. Chem. A* **122**, 843–848 (2018).
40. Tuttle, M. R., Davis, S. T. & Zhang, S. Synergistic effect of hydrogen bonding and π–π stacking enables long cycle life in organic electrode materials. *ACS Energy Lett.* **6**, 643–649 (2021).
41. Liang, Y. et al. A matrix-confined molecular layer for perovskite photovoltaic modules. *Nature* **648**, 91–96 (2025).
42. Stolterfoht, M. et al. The impact of energy alignment and interfacial recombination on the internal and external open-circuit voltage of perovskite solar cells. *Energy Environ. Sci.* **12**, 2778–2788 (2019).
43. Warby, J. et al. Mismatch of quasi-Fermi level splitting and V_{oc} in perovskite solar cells. *Adv. Energy Mater.* **13**, 202303135 (2023).
44. Johnson, S. et al. How non-ohmic contact-layer diodes in perovskite pinholes affect abrupt low-voltage reverse-bias breakdown and destruction of solar cells. *Joule* **9**, 102102 (2025).
45. Diekmann, J. et al. Determination of mobile ion densities in halide perovskites via low-frequency capacitance and charge extraction techniques. *J. Phys. Chem. Lett.* **14**, 4200–4210 (2023).
46. Kühne, T. D. et al. CP2K: an electronic structure and molecular dynamics software package - quickstep: efficient and accurate electronic structure calculations. *J. Chem. Phys.* **152**, 194103 (2020).
47. van Setten, M. J. et al. The PseudoDojo: Training and grading a 85 element optimized norm-conserving pseudopotential table. *Comput. Phys. Commun.* **226**, 39–54 (2018).
48. Lu, T. A comprehensive electron wavefunction analysis toolbox for chemists, Multiwfn. *J. Chem. Phys.* **161**, 082503 (2024).
49. Lu, T. & Chen, F. Multiwfn: a multifunctional wavefunction analyzer. *J. Comput. Chem.* **33**, 580–592 (2011).
50. Humphrey, W., Dalke, A. & Schulten, K. VMD: Visual Molecular Dynamics. *J. Mol. Graph.* **14**, 33–38 (1996).
51. Delley, B. An all-electron numerical method for solving the local density functional for polyatomic molecules. *J. Chem. Phys.* **92**, 508–517 (1990).
52. Perdew, J. P., Burke, K. & Ernzerhof, M. Generalized gradient approximation made simple. *Phys. Rev. Lett.* **77**, 3865–3868 (1996).
53. Goerigk, L. & Grimme, S. A thorough benchmark of density functional methods for general main group thermochemistry, kinetics, and noncovalent interactions. *Phys. Chem. Chem. Phys.* **13**, 6670–6688 (2011).
54. Johnson, E. R., Mackie, I. D. & DiLabio, G. A. Dispersion interactions in density-functional theory. *J. Phys. Org. Chem.* **22**, 1127–1135 (2009).
55. Kim, K.-H. et al. Phosphorescent dye-based supramolecules for high-efficiency organic light-emitting diodes. *Nat. Commun.* **5**, 4769 (2014).
56. Thompson, A. P. et al. LAMMPS - a flexible simulation tool for particle-based materials modeling at the atomic, meso, and continuum scales. *Comput. Phys. Commun.* **271**, 108171 (2022).
57. Rappe, A. K., Casewit, C. J., Colwell, K. S., Goddard, W. A. & Skiff, W. M. UFF, a full periodic table force field for molecular mechanics and molecular dynamics simulations. *J. Am. Chem. Soc.* **114**, 10024–10035 (2002).

58. Swope, W. C., Andersen, H. C., Berens, P. H. & Wilson, K. R. A computer simulation method for the calculation of equilibrium constants for the formation of physical clusters of molecules: application to small water clusters. *J. Chem. Phys.* **76**, 637–649 (1982).
59. Hoover, W. G. Canonical dynamics: equilibrium phase-space distributions. *Phys. Rev. A* **31**, 1695–1697 (1985).
60. Hockney, R. W. & Eastwood, J. W. *Computer Simulation Using Particles* (CRC Press, 1966).

Acknowledgements

M.S. acknowledges funding support from The Chinese University of Hong Kong (CUHK) through the Vice-Chancellor Early Career Professorship Scheme, the Research Grants Council (RGC) under the NSCF/RGC Joint Research Scheme (N_CUHK414/24) and Young CRF scheme (C4069-25YF), and the Innovation and Technology Commission (ITC) via the ITF Seed Fund (ITS/239/23). A.K.Y.J. thanks the sponsorship of the Lee Shau-Kee Chair Professor (Materials Science), the MHKJFS grant (MHP/054/23), TCFS grant (GHP/121/22SZ), and MRP grant (MRP/040/21X) from the Innovation and Technology Commission of Hong Kong, and the GRF grants (11307621, 11316422, 11308625) and CRS grants (CRS_CityU104/23, CRS_HKUST203/23) from the Research Grants Council of Hong Kong. This work was partially supported by City University of Hong Kong (9610739) for the project 'Fostering Innovation for Resilience and Sustainable Transformation,' officially endorsed by the United Nations Educational, Scientific, and Cultural Organization under the International Decade of Sciences for Sustainable Development (2024–2033).

Author contributions

Q.F., X.H., K.-K.L. and M.S. conceived the project. Q.F. and X.H. performed the experiments, analysed data and contributed to manuscript preparation. K.-K.L. designed and synthesized the molecules and conducted material characterizations. D.W. optimized device performance, S.Y. carried out the calculations and Z.S. conducted the GIWAXS measurements. Z.Lo., Z.Li., N.K., W.J., X.W., S.Z. and Z.Z. assisted with data interpretation and analysis. B.W. provided ToF-SIMS characterization. X.H., A.J. and M.S. finalized the manuscript with contributions from all authors.

Competing interests

M.S. is a co-founder of SolarSense Technologies Limited. The other authors declare no competing interests.

Additional information

Supplementary information The online version contains supplementary material available at https://doi.org/10.1038/s41560-026-02015-8.

Correspondence and requests for materials should be addressed to Xiaofeng Huang, Alex K.-Y. Jen or Martin Stolterfoht.

Peer review information *Nature Energy* thanks Hong Li and the other, anonymous, reviewer(s) for their contribution to the peer review of this work. Peer reviewer reports are available.

Reprints and permissions information is available at www.nature.com/reprints.

Publisher's note Springer Nature remains neutral with regard to jurisdictional claims in published maps and institutional affiliations.

[1]Electronic Engineering Department, The Chinese University of Hong Kong, Shatin, China. [2]Department of Materials Science and Engineering, City University of Hong Kong, Kowloon, China. [3]Hong Kong Institute for Clean Energy, City University of Hong Kong, Kowloon, China. [4]Shanghai Synchrotron Radiation Facility, Shanghai Advanced Research Institute, Chinese Academy of Sciences, Shanghai, China. [5]Department of Chemistry, City University of Hong Kong, Kowloon, China. [6]School of Chemistry and Molecular Engineering, East China University of Science and Technology, Shanghai, China. [7]Pen-Tung Sah Institute of Micro-Nano Science and Technology, Xiamen University, Xiamen, China. [8]State Key Laboratory of Marine Environmental Health, City University of Hong Kong, Kowloon, China. [9]These authors contributed equally: Qifan Feng, Kai-Kai Liu, Deng Wang. ✉e-mail: xhuan7@cityu.edu.hk; alexjen@cityu.edu.hk; mstolterfoht@ee.cuhk.edu.hk

nature portfolio

Corresponding author(s): Xiaofeng Huang, Alex K.-Y. Jen, Martin Stolterfoht

Solar Cells Reporting Summary

Nature Portfolio wishes to improve the reproducibility of the work that we publish. This form is intended for publication with all accepted papers reporting the characterization of photovoltaic devices and provides structure for consistency and transparency in reporting. Some list items might not apply to an individual manuscript, but all fields must be completed for clarity.

For further information on Nature Research policies, including our data availability policy, see Authors & Referees.

Experimental design

Please check the following details are reported in the manuscript, and provide a brief description or explanation where applicable.

1. Dimensions

Area of the tested solar cells	☒ Yes ☐ No	A shadow mask with an aperture area of 0.068 cm2 (0.0875 cm2 unmasked) is used for J-V measurements.
		Explain why this information is not reported/not relevant.
Method used to determine the device area	☒ Yes ☐ No	The mask area wsa confirmed with an optical microscope.
		Explain why this information is not reported/not relevant.

2. Current-voltage characterization

Current density-voltage (J-V) plots in both forward and backward direction	☒ Yes ☐ No	Figure 1J and throughout the Supplementary Information.
Voltage scan conditions	☒ Yes ☐ No	We used scan speeds of 200 and 500 mV/s for standard light and wider-range reverse J-V measurements, respectively. For fast-hysteresis (FH) measurements, the scan speed was varied from 0.1V/s to above 1000V/s using a triangular voltage pulse applied in both backward and forward directions, as described in the Methods section. To validate the FH results at slow scan rates (100–300 mV/s), conventional J–V measurements were performed on the same devices using a Keithley 2400, yielding performance metrics essentially identical to those obtained from the FH setup. Specified in Methods.
		Explain why this information is not reported/not relevant.
Test environment	☒ Yes ☐ No	Unless otherwise specified, all J–V scans, including measurements using the fast-hysteresis setup, were conducted at approximately 25 °C in a nitrogen-filled glovebox.
		Explain why this information is not reported/not relevant.
Protocol for preconditioning of the device before its characterization	☐ Yes ☒ No	*Provide a description of the protocol.*
		No preconditioning is used before standard JV characterization.
Stability of the J-V characteristic	☒ Yes ☐ No	The stability of the light JV is for example provided in Figure 1I, which shows a small hysteresis between forward (25.62%) and reverse scan (26.11%), respectively. The longer term stability under MPP tracking is provided in Figure 4C for up to 3000 h (1sun, 45 °C, encapsulated device outside a glovebox).
		Explain why this information is not reported/not relevant.

3. Hysteresis or any other unusual behaviour

Description of the unusual behaviour observed during the characterization	☐ Yes ☒ No	*Provide a description of hysteresis or any other unusual behaviour observed during the characterization.*
		No anomalous behavior was observed during characterization.
Related experimental data	☒ Yes ☐ No	Figure 1 and throughout the Supplementary Information.
		Explain why this information is not reported/not relevant.

4. Efficiency

External quantum efficiency (EQE) or incident photons to current efficiency (IPCE)

☐ Yes
☒ No

Provide a description of the technique used.

EQE data are not included because the study does not introduce conceptually new devices with exceptional performance, but instead focuses on the analysis of perovskite device stability.

A comparison between the integrated response under the standard reference spectrum and the response measure under the simulator

☐ Yes
☒ No

State where this information can be found in the text.

EQE data are not included because the study does not introduce conceptually new devices with exceptional performance, but instead focuses on the analysis of perovskite device stability. However, the current densities of device are in good agreement between measurements obtained in our laboratory and those certified by an independent institution.

For tandem solar cells, the bias illumination and bias voltage used for each subcell

☐ Yes
☒ No

Provide a description of the measurement conditions.

No tandem solar cells in this manuscript.

5. Calibration

Light source and reference cell or sensor used for the characterization

☒ Yes
☐ No

A silicon reference solar cell calibrated by the National Renewable Energy Laboratory (NREL), equipped with a KG-2 filter, was used, as specified in the Methods.

Explain why this information is not reported/not relevant.

Confirmation that the reference cell was calibrated and certified

☒ Yes
☐ No

The reference silicon solar cell was certified by National Renewable Energy Laboratory (NREL). Specified in Methods.

Explain why this information is not reported/not relevant.

Calculation of spectral mismatch between the reference cell and the devices under test

☐ Yes
☒ No

Provide a value of the spectral mismatch and/or a description of how it has been taken into account in the measurements.

No spectral mismatch calculation was performed.

6. Mask/aperture

Size of the mask/aperture used during testing

☒ Yes
☐ No

Aperture mask of 0.068 cm2 was used during testing.

Explain why this information is not reported/not relevant.

Variation of the measured short-circuit current density with the mask/aperture area

☐ Yes
☒ No

Report the difference in the short-circuit current density values measured with the mask and aperture area.

No significant variation was observed.

7. Performance certification

Identity of the independent certification laboratory that confirmed the photovoltaic performance

☒ Yes
☐ No

The device performance was certified by the Tianjin Institute of Metrological Supervision and Testing, yielding a PCE of 26.32%, which is consistent with the value obtained from laboratory measurements.

Explain why this information is not reported/not relevant.

A copy of any certificate(s)

☒ Yes
☐ No

Copies of the certificates are provided in Supplementary Figure 17.

Explain why this information is not reported/not relevant.

8. Statistics

Number of solar cells tested

☒ Yes
☐ No

Five individual devices were used for reverse-bias stability testing.

Statistical analysis of the device performance

☒ Yes
☐ No

This work focuses on perovskite device stability, with reverse-bias statistics from five individual devices shown in Supplementary Fig. 66.

Explain why this information is not reported/not relevant.

9. Long-term stability analysis

Type of analysis, bias conditions and environmental conditions

☒ Yes
☐ No

Operational stability, reverse-bias stability, and thermal stability tests are presented in Fig. 4C, Fig. 4D-H, and Fig. 4I, respectively.

Explain why this information is not reported/not relevant.